Key Points:
- Seasonal wind anomaly regions are defined as locations where the strongest winds do not coincide with the winter storm season
- Local winds influence significant wave height within seasonal wind anomaly regions
- Seasonal wind anomaly regions in the Southern Hemisphere are less influenced by local winds than those in the Northern Hemisphere

Supporting Information:

Supporting Information may be found in the online version of this article.

Correspondence to:

L. V. Colosi,
lcolosi@ucsd.edu

The Seasonal Cycle of Significant Wave Height in the Ocean: Local Versus Remote Forcing

Luke V. Colosi[1] , **Ana B. Villas Bôas[1]** , and **Sarah T. Gille[1]**

[1]Scripps Institution of Oceanography, University of California San Diego, La Jolla, CA, USA

Abstract Significant wave height (SWH) stems from a combination of locally generated "wind-sea" and remotely generated "swell" waves. In the Northern and Southern Hemispheres, wave heights typically undergo a sinusoidal annual cycle, with larger SWH in winter in response to seasonal changes in high-latitude storm patterns that generate equatorward propagating swell. However, some locations deviate from this hemispheric-scale seasonal pattern in SWH. For example, in the California coastal region, local wind events occur in boreal spring and summer, leading to a wind speed (WSP) annual cycle with a distinct maximum in boreal spring and a corresponding local response in SWH. Here ocean regions with a WSP annual cycle reaching a maximum in late spring, summer, or early fall are designated as seasonal wind anomaly regions (SWARs). Intra-annual variability of surface gravity waves is analyzed globally using two decades of satellite-derived SWH and WSP data. The phasing of the WSP annual cycle is used as a metric to identify SWARs. Global maps of probability of swell based on wave age confirm that during the spring and summer months, locally forced waves are statistically more likely in SWARs than in surrounding regions. The magnitude of the deviation in the SWH annual cycle is determined by the exposure to swell and characteristics of the wave field within the region. Local winds have a more identifiable impact on Northern Hemisphere SWARs than on Southern Hemisphere SWARs due to the larger seasonality of Northern Hemisphere winds.

Plain Language Summary At the ocean surface, wave height can give insight into ocean-atmosphere interactions. Storms generate waves, which are known as swell when they propagate away from their point of origin. Swell waves account for most of the global ocean's surface waves. They vary annually, with large waves in the winter and small waves in the summer, due to seasonal changes in high-latitude storm systems. In some coastal areas, including the coast of California, local wind effects cause exceptionally high wind speeds in late spring compared to other regions. These strong local winds result in large waves in springtime, separate from the global-scale winter maximum in swell waves. Places with strong local winds during the late spring, summer, and early fall are identified using global satellite observations of wave height and wind speed. Details vary by location. Wave fields in atypical wind regions depend on the exposure to swell as well as the strength of the local winds. Compared with Southern Hemisphere storms, Northern Hemisphere storms have a stronger winter peak. Therefore, local winds have a larger influence on atypical wind regions located in Northern Hemisphere than in Southern Hemisphere.

1. Introduction

Surface gravity waves are fundamental to ocean-atmosphere interactions, and they mediate exchanges of momentum, heat, gasses, and energy (Cavaleri et al., 2012; Edson et al., 2007; Sullivan et al., 2004; Villas Bôas et al., 2019). Surface winds generate wind waves, which are commonly defined as having wave periods from 1 to 30 s (Munk, 1951). These waves can propagate long distances across the oceans away from their generation site (Snodgrass et al., 1966). The wave field in a particular location represents the superposition of locally forced waves, "wind-sea," and remotely forced waves, "swell" (Chen et al., 2002; Jiang & Chen, 2013; Sverdrup & Munk, 1947; Villas Bôas et al., 2017).

Numerous studies have explored the importance of the seasonality of wind and wave climates. The annual and semi-annual cycles contain the majority of global wave and wind field variance (Stopa, 2019), which makes these cycles important for wind and wave climate studies. Better understanding wind and wave seasonality can improve predictions of the wind and wave climate and support marine engineering and

transportation efforts (Echevarria et al., 2019; Stopa, 2019; Young, 1999). Previous studies of the wave climate have focused both on the global scale, for example, by exploring the large-scale temporal trends and climate modes of the global wind and wave fields (e.g., Carter et al., 1991; Echevarria et al., 2019; Stopa, 2019; Stopa & Cheung, 2014; Young, 1999; Young et al., 2011) or by separating the wave field into swell and wind-sea components (e.g., Chen et al., 2002; Jiang & Chen, 2013; Semedo et al., 2011; Zheng et al., 2016) and regional scales (e.g., Semedo, 2018; Stopa et al., 2016; Villas Bôas et al., 2017; Young et al., 2020). Here, we focus on wind and wave seasonality on a regional scale to help fill gaps in our understanding of how local atmospheric conditions influence the variability of the wave field.

Previous research, including studies by Semedo (2018), Semedo et al. (2011), and Zheng et al. (2016), has relied on wave model hindcasts to look at the characteristics of the global wave field for swell and wind-seas. In the present study, our goal is to provide an alternative observation-driven approach for exploring the influence of locally and remotely forced waves on the wave field at the global and regional scales.

Villas Bôas et al. (2017) showed that regional-scale wind variability can cause deviations in the seasonal cycle of significant wave height (SWH). They explored a distinct deviation occurring off the California coast due to a local wind phenomenon known as expansion fan winds, which are generated by a combination of atmospheric conditions and coastal topography configuration (Winant et al., 1988). In the California Current region, expansion fan winds cause the wind speed (WSP) annual cycle to have a distinct maximum during late spring and early summer, which lies outside the timing of the expected hemispheric-scale annual cycle. As a result, locally generated waves dominate the wave field up to 50% of the time during late spring and early summer, causing a seasonal augmentation in SWH relative to the expected background SWH. Winant et al. (1988) hypothesized analogous wind events to be present in other oceanic regions that have coastal topography and atmospheric conditions similar to California and that may have similar WSP annual cycle variability. These regions include the west coast of Australia, the coast of Namibia, the coast of Chile, the southern Caribbean sea, the northwest coast of Africa near Morocco, and the Arabian Sea near the tip of Somalia. This list includes eastern boundary current regions, monsoon regions, and regions significantly sheltered from remotely forced waves. Here, we refer to ocean regions that have a WSP annual cycle reaching a maximum during the late spring, summer, or early fall collectively as Seasonal Wind Anomaly Regions (SWARs). To our knowledge, there has been no exploration of the possible influence of regional-scale wind variability on the intra-annual variability of SWH in SWARs.

In this study, we identify SWARs globally and assess whether the seasonality seen in the California Current region is typical of other SWARs, characterized by local effects that are out of sync with high-latitude winter storms. Global-scale satellite observations of SWH and WSP from 1993 to 2015 are used to identify the WSP seasonal cycle, and SWARs are identified based on the timing of this cycle relative to the expected hemispheric-scale annual cycle of WSP. Implications for wave climate are then assessed from the relative timing of the WSP and SWH seasonal cycles. The work presented here contributes to the current understanding of the wave climate in regions that are partially dominated by wind-seas, which may have relevance for sea-state dependent air-sea fluxes (Villas Bôas et al., 2019), management of coastal resources, as well as shipping and navigation (Ardhuin et al., 2019; Stopa, 2019).

This paper is organized as follows: Section 2 describes the data sets and methods used to analyze global SWH and WSP. Section 3 explores the parameters of the annual and semi-annual SWH and WSP least-squares models globally and regional climatologies of potential expansion fan wind SWARs. This section also examines whether SWH measurements during the late spring, summer or early fall months within SWARs are caused by locally or remotely generated waves. Section 4 summarizes our conclusions.

2. Data and Methods

2.1. Remotely Sensed Data

Wave data used in this study are drawn from over two decades (January 1, 1993–December 31, 2015) of cross-calibrated satellite altimeter SWH measurements produced by the Institut français de recherche pour l'exploitation de la mer (IFREMER) (Queffeulou, 2004; Queffeulou & Croizé-Fillon, 2017). IFREM-ER's SWH altimeter data set ensures near homogeneity of SWH measurements between multiple near-pole non-sun-synchronous satellites, which are calibrated against buoy observations. Here, we binned the daily

along-track data onto a 1° by 1° spatial grid. Satellites incorporated in this IFREMER product include ERS-1&2, TOPEX-Poseidon, GEOSAT Follow-ON, Jason-1, Jason-2, ENVISAT, Cryosat and SARAL AltiKa (see Queffeulou, 2004; Queffeulou & Croizé-Fillon, 2017). Recently, Dodet et al. (2020) has expanded and enhanced the time limited Queffeulou and Croizé-Fillon (2017) data set through the Sea State Climate Change Initiative. For the purposes of this study, Queffeulou and Croizé-Fillon (2017) provides data of sufficient quality and time length and is used here instead of Dodet et al. (2020).

Sea surface wind data were obtained from the Cross Calibrated Multi-Platform version 2 (CCMP2) wind vector analysis produced by Remote Sensing Systems (Atlas et al., 2011). CCMP2's data product is released on a 0.25° by 0.25° spatial grid with 6 hourly temporal resolution. For this analysis, we averaged CCMP2 winds spatially to a 1° by 1° grid and temporally to daily resolution in order to match the gridded SWH data. The CCMP2 product incorporates measurements from scatterometers, radiometers, in situ buoys, and modeled wind velocity. CCMP2 provides zonal and meridional components of winds 10 meters above the sea surface, which are used to compute WSP (Atlas et al., 2011).

2.2. WAVEWATCH 3 Model Hindcast

To complement our satellite data analysis, we use a wave hindcast produced by IFREMER using the WAVE-height, WATer depth and Current Hindcasting III (WW3) wave model forced by Climate Forecast System Reanalysis (CFSR) winds. Simulations span the period from 1993 to 2015 and are output at 6 hourly temporal and 0.5° spatial resolution. For model setup and validation, we refer the reader to Rascle and Ardhuin (2013). In the supporting information, we show our core analyses repeated with WW3 SWH and CFSR WSP (Figures S1–S2).

2.3. Monthly Climatology: Annual and Semi-Annual Variability

The analysis in this study focuses on annual and semi-annual variability as well as the mean states of the wave and wind fields using monthly averaged SWH and WSP. In order to analyze the annual and semi-annual variability, at each grid point, we perform a weighted least-squares fit to the mean, annual, and semi-annual cycles of SWH and WSP monthly climatologies, following closely the analysis from Carter et al. (1991). Annual and semi-annual cycles are represented as a sum of a sine and cosine, and fitted coefficients are used to infer amplitude and phase. See Figure S3 for an example of the annual and semi-annual sinusoidal components of the model for SWH in the Southern Caribbean SWAR. A sinusoidal representation of the annual and semi-annual cycles is used as a first-order approximation of this variability. In the supporting information, we show our annual and semi-annual cycle model fitted to monthly climatologies in seven SWAR regions (Figure S4) to illustrate statistical skill. See Stopa (2019) for a non-parametric approach to represent the annual and semi-annual cycles without imposing the forms of a sine or cosine. Since 5 coefficients were least-squares fitted, IFREMER SWH grid locations were considered only if climatological means were available for at least 5 months of the year. In addition, to reduce errors associated with sparse sampling, we required that there be at least one climatological monthly mean in each of the four seasons. For weights, we use the standard error of the monthly climatology mean SWH and WSP. The number of independent observations for each monthly climatology average was computed using the decorrelation time scale over each month of CCMP2 WSP and IFREMER SWH daily data. Decorrelation time scales are computed from integrals of the lagged covariance (e.g., Gille, 2005), as discussed in the Supporting Information S1. As a metric to evaluate the least-squares fit, we use fraction of variance explained (FVE) (Draper & Smith, 1998), defined as:

$$\text{FVE} = 1 - \frac{\sum_{i=1}^{N}\left(\dfrac{y_i - f_i}{\delta y_i}\right)^2}{\sum_{i=1}^{N}\left(\dfrac{y_i - \mu}{\delta y_i}\right)^2}, \tag{1}$$

where y_i is the ith monthly climatology mean data point with standard error δy_i, μ is the mean derived from the weighted least-squares fit of the data, and f_i is the ith model value. Data and model are weighted in Equation 1 for consistency with the weighted least-squares fit. Since the weights represent the standard error of the mean,
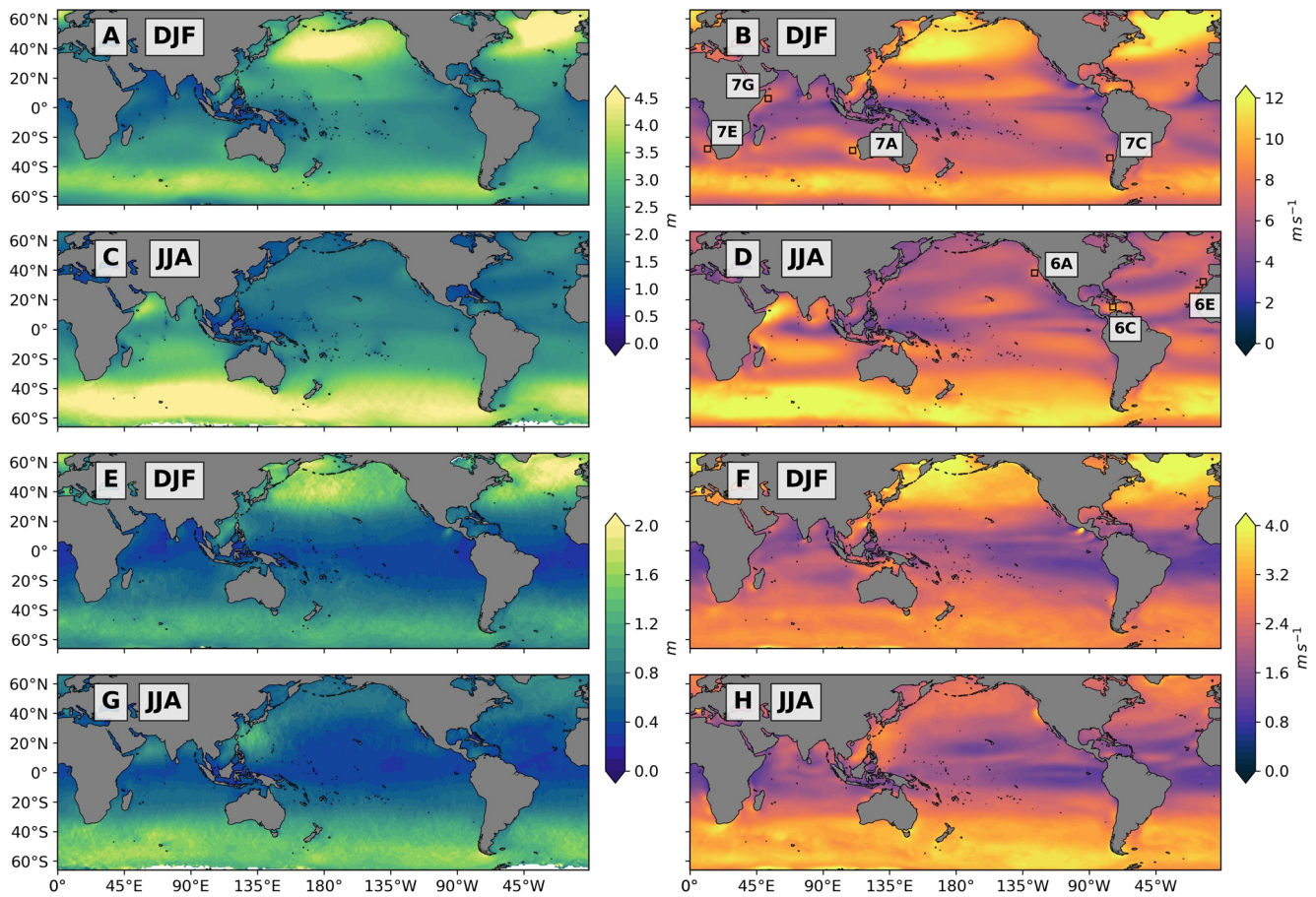
Figure 1. December-January-February (DJF) seasonal mean for (a) Institut français de recherche pour l'exploitation de la mer significant wave height (IFREMER SWH) and (b) Cross Calibrated Multi-Platform version 2 wind speed (CCMP2 WSP); June-July-August (JJA) seasonal mean for (c) IFREMER SWH and (d) CCMP2 WSP; DJF standard deviation of daily data for (e) IFREMER SWH and (f) CCMP2 WSP; JJA standard deviation of daily data for (g) IFREMER SWH and (h) CCMP2 WSP. See text for details of computation. Black boxes next to 6A,C,E and 7A,C,E,F labels in panels (b) and (d) indicate the regions selected for monthly climatology analysis in the Southern and Northern Hemispheres, respectively.

uncertainties inferred from the least-squares fit (e.g., Press et al., 1992) can be interpreted as the standard error of the mean of each fitted coefficient. Statistical uncertainties of the amplitude are computed using error propagation and thus represent the standard error of the mean amplitude. Amplitudes smaller than twice the standard error were judged not to be statistically different from zero. At grid points where the amplitude is not statistically significant, the phase is considered not well defined. The regions identified as having statistically significant annual and semi-annual cycles of SWH and WSP are relatively insensitive to small changes in the statistical significance criteria. See Figure S5 for fractional uncertainty for SWH and WSP amplitude.

Maps of the mean and standard deviation of SWH and WSP daily data in December-January-February (DJF) and in June-July-August (JJA) illustrate the seasonal evolution and variance of the data (Figure 1). Monthly SWH and WSP climatologies were computed for candidate expansion fan regions identified by Winant et al. (1988) by spatially averaging monthly climatologies and their variances within 4° by 4° regions. These regions are outlined by black boxes located next to the region labels (6A,C,E and 7A,C,E,F) in Figures 1b and 1d. We selected 4° by 4° regions with anomalously high WSP, small spatial WSP gradients, and annual cycle phases corresponding to WSP maxima during the late spring, summer, or early fall. To minimize the effects of land contamination for satellite altimetry SWH data, 4° by 4° regions are at least 1° of longitude and latitude away from the coast. Uncertainties for SWH and WSP monthly climatologies were computed by dividing the standard deviation (σ) by $\sqrt{N_{\text{eff}}}$, where N_{eff} is the number of degrees of freedom, to obtain the standard error of the mean ($\sigma / \sqrt{N_{\text{eff}}}$). We estimated N_{eff} by averaging monthly temporal

decorrelation scales (n_d), representing the number of data points between statistically independent measurements, into monthly climatological averages, dividing the number of observations N used to compute the monthly climatological average by the decorrelation scale such that $N_{eff} = N / n_d$, and then spatially averaging N_{eff} over the 4° by 4° region. This approach assumes that the spatial variation does not contribute to the degrees of freedom.

Basin-scale SWH and WSP annual cycles were obtained for the Northern and Southern Hemispheres of the Pacific, Atlantic, and Indian Oceans through weighted least-squares fits of the monthly climatologies (see Figure S6 for basin-scale mean climatologies and annual cycle fits). In targeted study regions, we compare the regional SWH climatology to the basin-scale SWH annual cycle. To do this, we assume that the phasing of the SWH is determined on a basin-scale (largely by high-latitude storms), while the mean SWH and amplitude of the annual cycle can vary geographically. Thus we project the observed local SWH onto the basin-scale fitted annual cycle. Differences between the two quantify the deviation of the regional climatology from the expected hemispheric-scale annual cycle.

2.4. Definition of Seasonal Wind Anomaly Regions

The WSP annual-cycle phase, ϕ_{wsp}, allows us to identify atypical regions, where local winds are out of phase with hemispheric scale winds, providing a quantitative approach to identify SWARs. We define a SWAR as a region with a statistically significant WSP annual cycle amplitude, with a phase that differs by 2.5 or more months from the expected WSP phase ϕ_{exp} set by hemispheric large-scale storm systems,

$$\left| \phi_{wsp} - \phi_{exp} \right| \geq 2.5 \text{ months.} \tag{2}$$

Assuming that ϕ_{exp} corresponds to a WSP annual cycle reaching a maximum during the middle of winter, mid-January in the Northern Hemisphere and mid-July in the Southern Hemisphere, the criterion in Equation 2 is fulfilled when the WSP maximum occurs roughly from April through October (boreal late spring, summer and early fall) for the Northern Hemisphere and from October through April (austral late spring, summer, and early fall) for the Southern Hemisphere.

3. Results and Discussion

3.1. Annual and Semi-Annual Cycles in Wind Speed and Significant Wave Height

Annual cycle phase maps show that in many regions across the globe, including high-latitude oceans, the tropical Atlantic and Pacific, and the region north of New Zealand, SWH and WSP are in phase, implying that the annual maximum wave height coincides in time with annual maximum WSP. Generally, wind and waves both reach maxima in their annual cycles in winter in both hemispheres. An exception occurs in the northern Indian Ocean, which is sheltered from high-latitude Northern Hemisphere winter storms (Figures 2a and 2b). Several other regions stand out in Figures 2a and 2b as deviating from these general patterns, either because WSP or SWH does not peak in winter or because WSP and SWH are out of phase with each other.

The annual cycle amplitude of both SWH and WSP (Figures 2e and 2f) is larger in the high-latitude Northern Hemisphere than in the high-latitude Southern Hemisphere, implying more seasonal variability in wave height and winds in the Northern Hemisphere than in the Southern Hemisphere. However, seasonal mean SWH and WSP are consistently higher in the Southern Hemisphere (Figures 1a–1d). For SWH, high-amplitude annual cycles also occur in the Arabian Sea and in zonal bands from ~30°–45° in the Northern and Southern Hemispheres. In the tropical Pacific and Atlantic, the SWH amplitude drops to near zero, but the WSP annual amplitude does not approach zero in the same locations.

The semi-annual cycle phases for SWH and WSP (Figures 2c and 2d) have more spatial structure than the corresponding annual cycle phases. However, many grid points are judged not to be statistically significant (white pixels in Figures 2c and 2d). In regions with high-amplitude WSP and SWH semi-annual cycles,
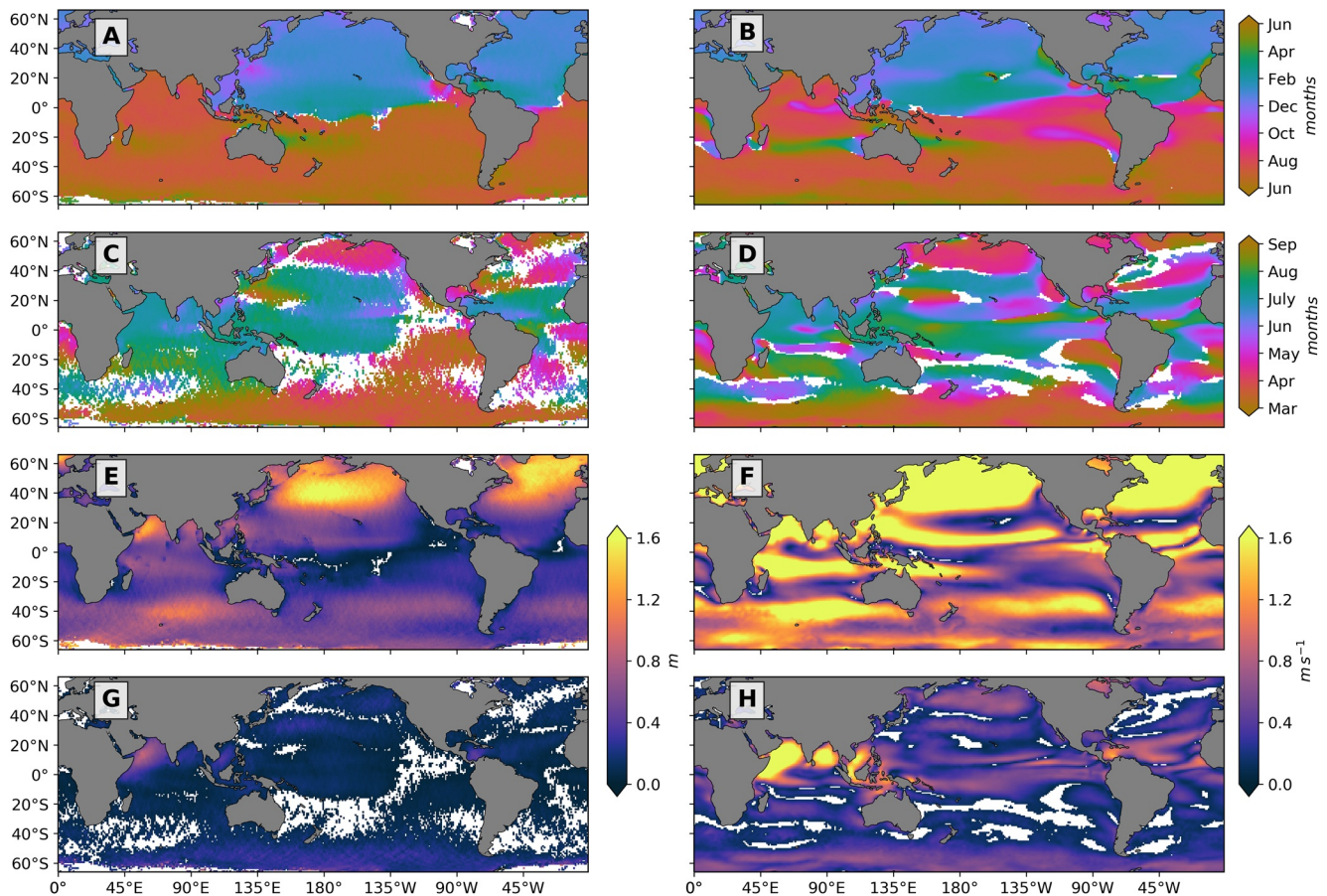
Figure 2. Phase of annual cycle for (a) Institut français de recherche pour l'exploitation de la mer significant wave height (IFREMER SWH) and (b) Cross Calibrated Multi-Platform version 2 wind speed (CCMP2 WSP); phase of semi-annual cycle for (c) IFREMER SWH and (d) CCMP2 WSP; amplitude of annual cycle for (e) IFREMER SWH and (f) CCMP2 WSP; amplitude of semi-annual cycle for (g) IFREMER SWH and (h) CCMP2 WSP. Amplitudes less than or equal to twice the standard error are not considered statistically significant and are masked white; the same pixels are also masked for phase. See Section 2.3 for details of computation. Phase is indicated in months. Streak patterns in A, C, E, and G are an artifact of the altimeter sampling patterns and should not be interpreted as robust signal. (Comparison plots showing equivalent quantities for WAVE-height, WATer depth and Current Hindcasting III (WW3) and IFREMER SWH and CFSR and CCMP2 WSP can be found in Figure S1).

including the Arabian Sea, Bay of Bengal, South China, and Southern Caribbean, WSP and SWH are in phase, with phase values indicating maxima or minima occurring in April and October.

The SWH and WSP semi-annual cycle amplitudes are smaller in magnitude than the annual cycles (Figures 2g and 2h). For both WSP and SWH, the regions with the highest amplitude semi-annual cycles occur in the Arabian and Southern Caribbean Seas. The Bay of Bengal and the South China Sea have high amplitude only for WSP. The South Asian monsoon's semi-annual occurrence may play a role in strong semi-annual cycles, as the Arabian Sea, the Bay of Bengal, and the South China Sea are all monsoon regions.

Global maps of FVE (Figures 3a and 3b) assess the percentage of the variance explained by the mean plus annual and semi-annual cycles for monthly averaged SWH and WSP respectively. Features in the FVE maps for SWH and WSP align with features in the SWH and WSP annual and semi-annual amplitude maps (Figures 2e and 2g): the percent of variance explained by the least-squares fit is highest in regions with high amplitude and lowest in regions that have near zero amplitude or that are considered not statistically significant. In locations where the annual and semi-annual cycles do not explain all of the temporal variability, local wind effects may be intermittent or simply governed by processes that are distinct from the annual and semi-annual cycle. In addition, variance unexplained by the model may be a result of imposing a sinusoidal shape to the annual and semi-annual cycle. We refer the reader to Stopa (2019) for more details on a non-parametric method for representing the annual cycle. Stopa (2019) also computed percent variance
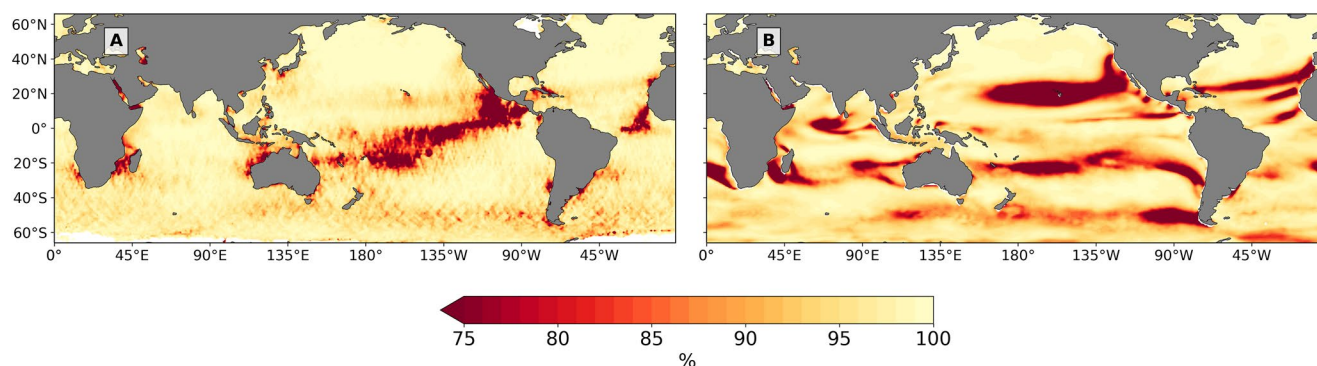
Figure 3. Fraction of variance explained by weighted annual and semi-annual least squares fit for Institut français de recherche pour l'exploitation de la mer significant wave height (IFREMER SWH) (a) and Cross Calibrated Multi-Platform version 2 wind speed (CCMP2 WSP) (b) from January 1, 1993 to December 31, 2015.

explained for WSP and SWH (Figures 1a and 1b in their paper), which is significantly lower than the FVE in our Figures 3a and 3b since we are fitting our model to monthly climatologies, while Stopa (2019) uses monthly averages.

3.2. Waves: Swell Phase Discontinuities

In the equatorial Pacific and Atlantic, SWH phasing shows a sharp discontinuity between the Northern Hemisphere (boreal winter maximum) and the Southern Hemisphere (austral winter maximum) (Figure 2a). This phase transition, which we will refer to as a "swell phase discontinuity" occurs in regions of low to moderate seasonal mean SWH (Figures 1a and 1c) and low standard deviation (Figures 1e and 1g). Because swell is primarily generated in winter, this identifies the transition between regions with swell originating primarily in the Northern Hemisphere and swell primarily from the Southern Hemisphere. The swell phase discontinuity roughly coincides geographically with "swell fronts" defined based on mean wave direction (Jiang & Chen, 2013; Semedo et al., 2011; Young, 1999). Young (1999) found that the Pacific and Atlantic swell front geographic locations vary seasonally. Since we define the swell phase discontinuity using SWH annual cycle phase, it represents an annually averaged signal that is, expected to align with the annually averaged position of the swell front.

The swell phase discontinuity is slightly south of the equator in the western Pacific, between 5°S and 10°S west of 170°W, and it shifts equatorward further east (Figure 2a). In the Atlantic, the swell phase discontinuity aligns closely with the equator in the western Atlantic and abruptly shifts north of the equator near the western coast of Africa. Factors other than swell may affect the SWH phase discontinuity. Explanations for the geographic location of these boundaries are beyond the scope of the study and will be left for future research.

Just south of the swell phase discontinuity in the equatorial Pacific, several abrupt shifts in phase exist between 10°S and 20°S at approximately 180°E and 145°W. These are located on the northward facing sides of islands and are consistent with island shadowing: waves from the Southern Ocean propagating northward encounter the topography of Polynesian islands and are blocked from traveling any further north. As a result, waves vary with the Southern Hemisphere seasonal cycle to the south of the islands, and vary with the Northern Hemisphere seasonal cycle to the north of the island (see Figure S7 for an enlarged map of the SWH annual cycle phase in the Polynesian island region).

3.3. Winds: Identifying Seasonal Wind Anomaly Regions

Candidate SWARs determined by Equation 2 are highlighted in Figure 4 (Figure S8 provides global maps of SWARs using alternate criteria.). For this analysis, marginal seas and the equatorial regions across the Pacific and Atlantic Oceans are not considered. SWARs largely agree with the potential expansion fan regions identified by Winant et al. (1988) with the exception of the Arabian Sea. This metric also identifies some
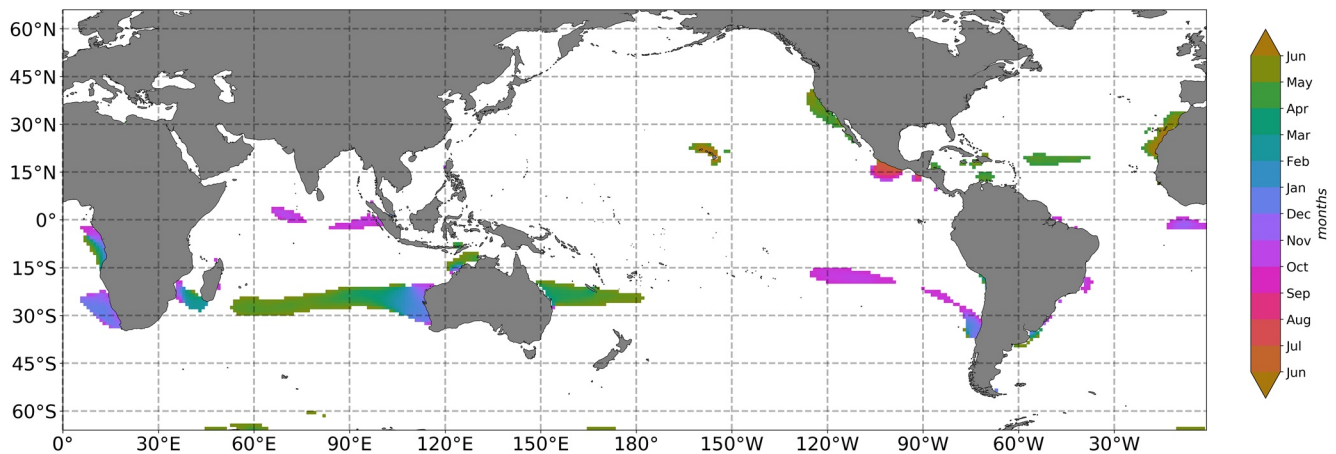
Figure 4. Annual cycle phase for Cross Calibrated Multi-Platform version 2 (CCMP2) wind speed (WSP), highlighting seasonal wind anomaly regions (SWARs) using the WSP maximum criteria. White pixels correspond to points that are not categorized as having anomalous phase or where the amplitude is not statistically significant.

regions that were not suggested by Winant et al. (1988), including the Central North and South Atlantic, the Central West African coast off Angola, the Southern Mozambique Channel, the North Indian Ocean, the Northwest and Eastern Australian coasts, Hawaii, the mid-latitude Southern Pacific, the Southern Mexican coast and multiple small coastal regions along the eastern South American coast. Table 1 categorizes candidate SWARs into three groups: expansion fan wind regions identified by Winant et al. (1988), coastal regions, and open ocean regions. In the Southern Hemisphere, SWARs are concentrated in a zonal band from 15°S–30°S. From 66°S to 66°N latitude, we found that SWARs constitute approximately 3.39% of the ocean's surface area. SWARs highlighted by this approach could be generated by a broad range of meteorological phenomena other than expansion fan wind events.

3.4. Wind and Wave Relationships

By comparing the timing of the annual cycle phases, ϕ_{swh} and ϕ_{wsp}, we explore the relationship between local winds and the regional wave field, as illustrated in Figure 5. In high latitudes, local winds are in phase with waves, consistent with storms generating waves. Near the swell phase discontinuity and in most SWAR regions, local winds and waves are out of phase. From 66°S to 66°N latitude, WSP and SWH phases differ by 0–1 month for 57.13% of the ocean's surface area, while phase differences range from ±4–6 months for 1.65% of the ocean's surface area.

The relationship between WSP and SWH annual cycle phases shows the impact of local winds on the wave field. We find two types of relationships: (a) waves aligned with hemispheric scale waves but out of phase with local winds, and (b) waves not aligned with hemispheric scale waves but in-phase with local winds.

Table 1
Candidate SWARs, Identified Using Equation 2, With Figure Number of SWAR's Regional Climatology

Expansion fan regions	Coastal	Open ocean
West Australian Coast (Figure 7a)	Central West African Coast (Figure S11b)	Central North Atlantic (Figure S10c)
Namibian Coast (Figure 7g)	Southern Mozambique Channel (Figure S11c)	Central South Atlantic (Figure S11a)
Chilean Coast (Figure 7c)	Northwest Australian Coast	North Indian Ocean (Figure S11e)
Southern Caribbean Sea (Figure 6c)	Eastern Australian Coast (Figure S11f)	Mid-latitude Southern Pacific (Figure S11d)
Northwest African Coast (Figure 6e)	Hawaii (Figure S10a)	
California Coast (Figure 6a)	Southern Mexican Coast (Figure S10b)	
	Eastern South American Coast	

Note. Expansion Fan regions are identified by Winant et al. (1988).
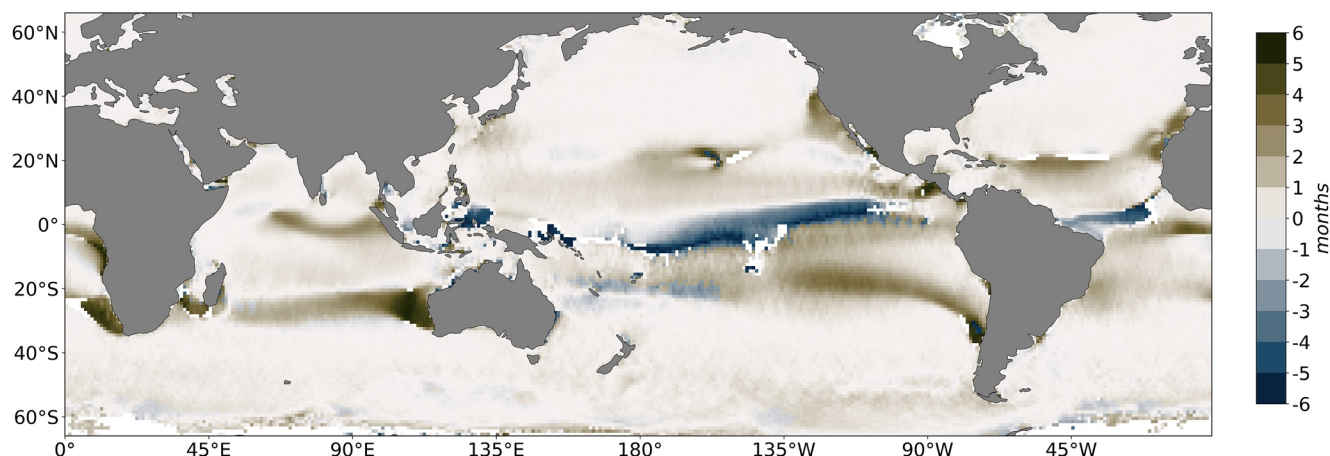
Figure 5. Difference between the annual cycle phases, ϕ_{wsp} and ϕ_{swh}. White pixels correspond to points where phase differences are not statistically significant, or where the annual cycle amplitude is small enough that phase is not well defined.

In most SWARs, ϕ_{swh} and ϕ_{wsp} differ by 2–6 months (Figure 5), so that mean WSP reaches a maximum when mean SWH is near its minimum. Villas Bôas et al. (2017) described such a phase relationship within the California Current SWAR, where the WSP maximum occurs during boreal spring or summer. Since annual cycles in SWH are usually attributed to swell, high local winds that are out of sync with remotely generated waves suggest the possibility of locally forced wind waves that peak at a different time of year than the swell generated in the same hemisphere as the SWAR. SWARs thus have the potential to have SWH that deviates from the annual cycle typical of swell originating from high-latitude storms. However, observations suggest that regional wave and wind characteristics may be important in determining the extent to which local winds influence the wave field. Three characteristics of primary importance include exposure to swell generated in the high-latitude Northern or Southern Hemisphere, swell's annual cycle amplitude, and the strength of local winds. Among all SWARs, there are regions that have no exposure to Northern or Southern Hemisphere swell, regions with exposure to swell from one hemisphere, and regions with exposure to both Northern and Southern Hemisphere swell. Different combinations of these three characteristics lead to local winds having varied impacts on the regional wave field. Deviations from the annual cycle could also be attributed to swell originating in the high latitudes of the opposite hemisphere such that contributions to SWH from opposing hemisphere swell are greater than locally generated wind-seas. Furthermore, compared with the Northern Hemisphere, the Southern Hemisphere's low SWH annual cycle amplitude (Figure 2e) provides relatively consistent swell, making regions with significant exposure to the Southern Hemisphere experience less measurable influence from local winds.

Exceptions to the out-of-phase behavior in SWARs occur in the Arabian Sea, the Eastern Australian Coast, the South Mexican Coast, and the Southern Caribbean, where ϕ_{wsp} and ϕ_{swh} have a 0–1 month phase difference. This in-phase relationship, along with ϕ_{swh} reaching a maximum outside the timing of the expected hemispheric SWH annual cycle (Figure 2a), suggests that the waves within these SWARs are primarily locally forced, with little impact from remotely forced swell.

3.5. Regional Climatologies of SWARs

In order to examine how phasing differences in the SWH and WSP annual cycles influence wave fields within SWARs, monthly climatologies for SWH and WSP were computed in 4° by 4° grid boxes centered on a core portion of the SWAR. Here we focus on SWARs in the potential expansion fan regions identified by Winant et al. (1988). Regional climatologies for all other SWARs can be found in the Supporting Information (see Figures S9–S11). Calculations use data from January 1, 1993 to December 31, 2015 and focus on the individual boxes outlined in Figures 1b and 1d with enlarged maps in the left panels of Figures 6 and 7. The right panels of Figures 6 and 7 show SWAR regional climatologies for WSP (solid red) and SWH (solid blue) for the Northern and Southern Hemispheres, with the hemispheric SWH mean annual cycle
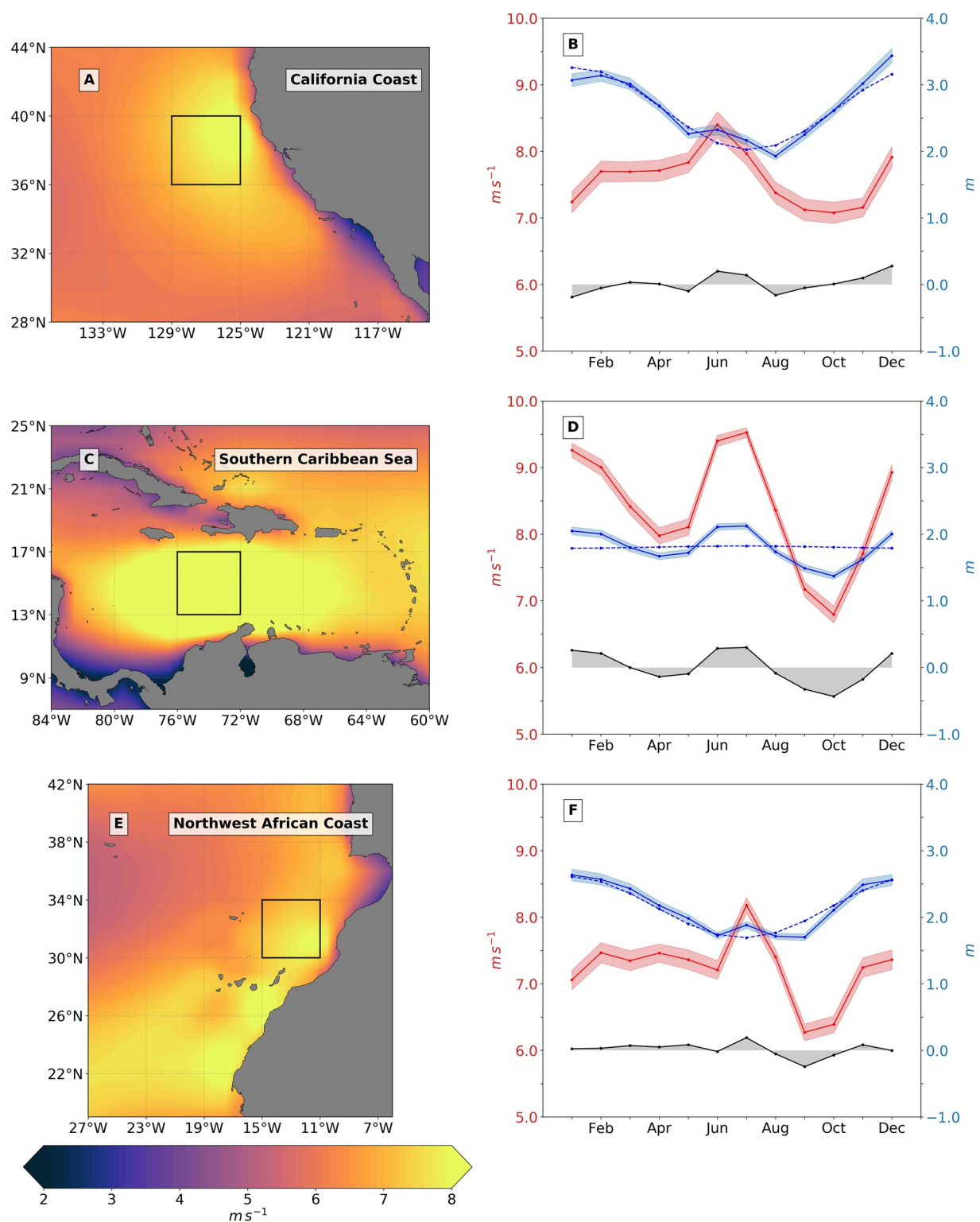
Figure 6.

computed as an average for the ocean basin (blue dashed line) and the residual between SWH climatology and basin-scale annual cycle (black, with gray shading). In Figures 6 and 7, WSP and SWH climatologies show distinctly different patterns depending on region. On the basin scale, with the exception of the Indian Ocean (which we will address separately), SWH and WSP exhibit nearly the same basin-scale annual cycles in each ocean basin (Figure S6). This means that regional deviations in SWH cannot be attributed to geographic variations in basin-scale wind climatologies.

For Northern Hemisphere SWARs in eastern boundary current regions (i.e., the California Current in Figures 6a and 6b and North Africa in Figures 6e and 6f), the sharp summer peak in the WSP climatology (red) coincides with an anomalous augmentation in SWH (blue) relative to the basin-scale annual cycle (blue dashed line). In both cases, the observed augmentations deviate by more than twice the standard error from the basin-scale annual cycle.

In contrast, in the Southern Hemisphere eastern boundary current areas, with the exception of western Australia (i.e., the Chilean coast in Figures 7c and 7d and the Namibian coast in Figures 7e and 7f), we see broad summer increases in WSP extending from October or November through February or March (red) that correspond to small magnitude deviations of SWH (blue) of less than 0.5 standard errors from the basin-scale annual cycle. These results imply that in Southern Hemisphere SWARs (Figure 7), local winds have comparatively less influence on the wave climate than in the Northern Hemisphere, possibly because strong year-round winds in the high-latitude Southern Hemisphere lead to a smaller seasonal cycle in Southern Hemisphere swell (Figure 2a) and more overall wave energy than in the Northern Hemisphere. Against this background level of wind and swell, locally induced anomalies in the Southern Hemisphere are expected to be less distinct than in the Northern Hemisphere. The Indian Ocean is unusual in displaying a basin-scale WSP maximum in the austral summer months in addition to an austral winter maximum, which complicates interpretation of processes governing SWAR WSP and SWH. Off the coast of Western Australia (Figures 7a and 7b), the summer WSP peak that extends from December to February is particularly strong and corresponds to a 0.38 m SWH deviation (more than 3 standard errors) from the Indian Ocean's annual cycle. This is near the same magnitude as deviations in the Northern Hemisphere, suggesting that Western Australia's local winds are strong enough to influence the wave field at a level similar to Northern Hemisphere SWARs. The basin-scale WSP local maximum during austral summer may also play a role in determining the magnitude of the deviation.

The monsoon region in the Arabian Sea (Figures 7g and 7h) and the tropical storm region in the southern Caribbean Sea (Figures 6c and 6d) have distinctly different wind and wave climatologies than the eastern boundary current regions. Both regions are characterized by strong semi-annual cycles in WSP (red lines in Figures 6d and 7h), and by SWH that varies with the semi-annual WSP (blue lines in Figures 6d and 7h). In the Caribbean, SWH shows a smaller amplitude annual cycle (blue dotted line in Figure 6d) relative to semi-annual cycle amplitude, and in the Arabian Sea the annual cycle in SWH captures only a portion of the overall SWH variability. In both regions, the significance of the SWH semi-annual cycle compared with the annual cycle is demonstrated by the large deviations from the annual cycle (gray shading in Figures 6d and 7h). These patterns imply that semi-annually varying local winds are important drivers of SWH in these regions. The Antilles archipelago shelters the Southern Caribbean SWAR from waves propagating from high latitudes (Semedo et al., 2011) (Figure 6c). The lack of annual cycle in the SWH is consistent with the hypothesis that Caribbean SWH is forced entirely by local winds. In contrast, the Arabian Sea is not fully sheltered from remotely generated swell, and Indian Ocean WSP has a distinct pattern of semi-annual variability, meaning that SWH in the Arabian Sea could result from a combination of locally forced wind waves and remotely forced swell.

Figure 6. (left column) Northern Hemisphere wind speed in SWARs, averaged over June, July, and August. (right column) Institut français de recherche pour l'exploitation de la mer significant wave height (IFREMER SWH) (solid blue) and Cross Calibrated Multi-Platform version 2 wind speed (CCMP2 WSP) (solid red) climatologies extracted from the outlined 4° by 4° boxes within seasonal wind anomaly regions (SWARs). Blue shading represents the standard error of the mean, dotted blue is the annual cycle weighted least-squares fitted to monthly climatology for mean SWH of the hemisphere ocean basin the SWAR is located in, and black solid is the residual between SWH regional climatology and annual cycle. SWARs include Northern California (a) and (b), Southern Caribbean Sea (c) and (d), and North Africa near the coast of Morocco and western Sahara (e) and (f). (Comparison plots showing equivalent quantities for WW3 and IFREMER SWH and CFSR and CCMP2 WSP can be found in Figures S2a, S2c and S2e of the Supporting Information).
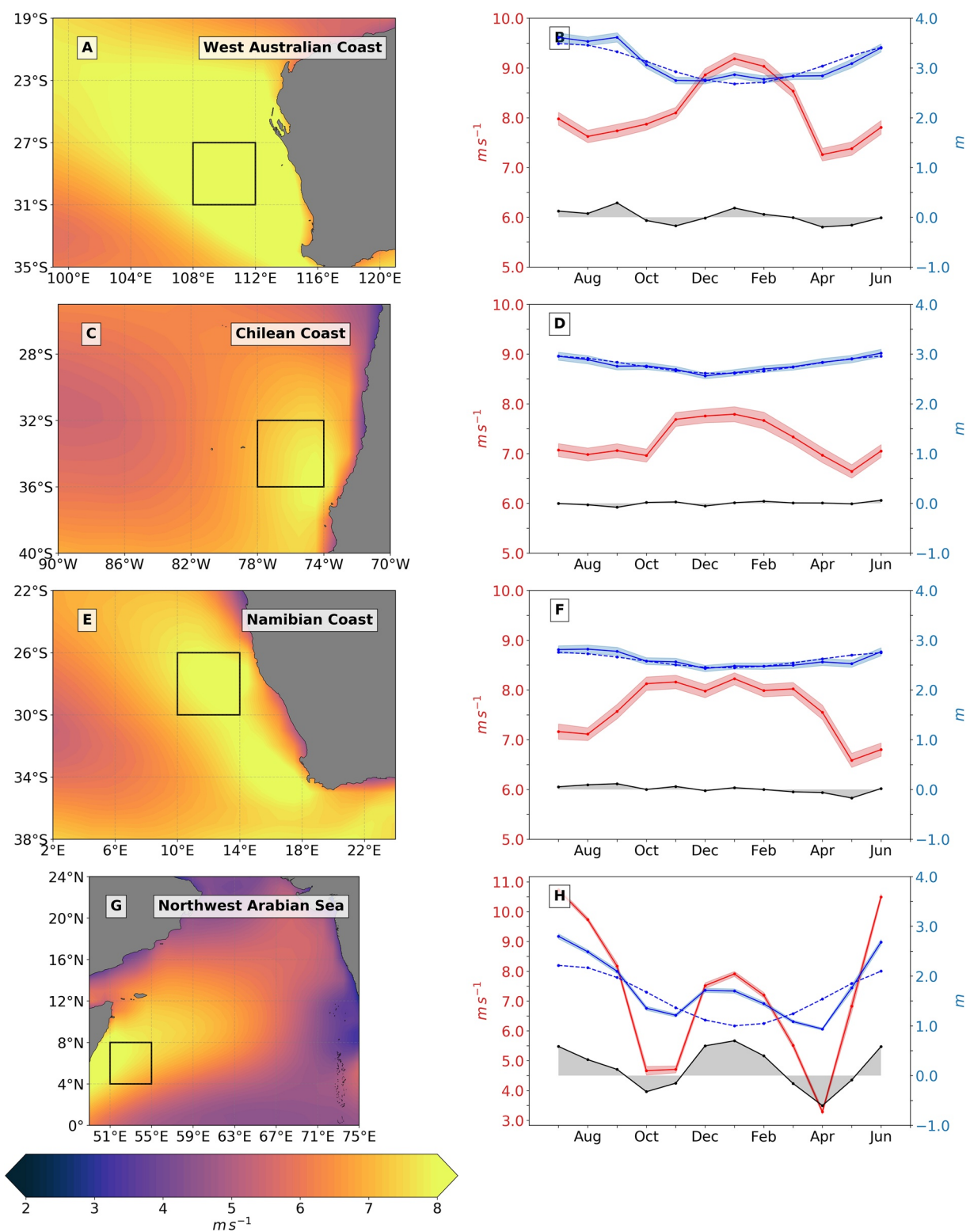
Figure 7.

3.6. Wind-Sea Versus Swell Dominance in SWARs

The phase differences and climatologies discussed in the preceding sections suggest the likely distinctions between remotely forced swell and locally forced wind waves. Phase differences between local SWH and hemispheric wind and wave climatologies can also occur if a region has significant exposure to swell propagating from the opposite hemisphere.

One method to distinguish swell from wind-sea is through wave age, which quantifies the stage of development of waves (Alves et al., 2003). The wave age criterion is defined, following Donelan et al. (1992), as:

$$\text{Wave Age} = \frac{C_p}{U_{10}}, \tag{3}$$

where C_p is the phase speed at the peak frequency of the wave spectrum, and U_{10} is the WSP at 10 m elevation. Here, we use an equivalent wave age, where the phase speed C_p is computed at the frequency associated with the mean period $T_{m0,1}$: $\langle f \rangle = 1 / T_{m0,1}$. The mean period $T_{m0,1}$ is defined by as the period computed from the first frequency moment of the wave spectrum (see Ardhuin, 2020). For $C_p / U_{10} \leq 1.2$, the wave field is assumed to be dominated by wind-sea and highly coupled to the local winds, with wind still supplying momentum to waves. For $C_p / U_{10} > 1.2$, the wave field is assumed to be dominated by swell, where waves traveling 20% faster than U_{10} are outrunning the wind and not receiving momentum from the wind. For deep water waves, which are the focus of this paper, with mean frequency $\langle f \rangle$, the dispersion relationship yields the phase speed:

$$C_p = \frac{g}{2\pi\langle f \rangle}. \tag{4}$$

The wave field can be composed of a superposition of multiple wave systems such that both swell and wind-sea may co-exist. The phase speed is computed using the mean period $T_{m0,1}$ to account for this. $T_{m0,1}$ is used instead of peak frequency f_p because f_p is a nosier parameter and $T_{m0,1}$ is a weighted average, which considers the distribution of energy across frequencies. See Figure S12 which compares the probability of swell from the DJF and JJA seasons with wave age computed using f_p, $T_{m0,1}$, and $T_{m0,-1}$ (Ardhuin, 2020). Although both swell and wind-sea are likely to co-exist in the wave field, this categorization assumes that the wave field is dominated either by swell or by wind-sea waves.

Using equivalent wave age, probability of swell can be obtained to estimate the fraction of time that the wave field is swell-dominated relative to the total number of wave measurements:

$$\text{Probability of swell} = \frac{N_{swell}}{N_{total}}, \tag{5}$$

where N_{swell} is the number of observations with wave age exceeding 1.2, representing a swell-dominated wave field, and N_{total} is the total number of observations in the time series. Probability of swell provides a metric to evaluate whether the atypical wind climatology within a SWAR is responsible for wind-seas during the late spring, summer, and early fall.

Previous global estimates of probability of swell (Jiang & Chen, 2013; Semedo et al., 2011; Zheng et al., 2016) have shown that remotely forced waves dominate the wave field in all ocean basins with the exception the Southern Ocean, some coastal regions, and common storm tracks, where wind-generated waves play a stronger role. Here, we complement their results by focusing on regional analysis of SWARs. For probability of swell calculations, we use mean period $T_{m0,1}$ and U_{10} from the WW3 hindcast. Figures S1 and S2 show that WW3 SWH annual cycles resemble IFREMER SWH annual cycles.

Figure 7. (left column) Southern Hemisphere wind speed in seasonal wind anomaly regions (SWARs), averaged December, January, and February with (right column) Institut français de recherche pour l'exploitation de la mer significant wave height (IFREMER SWH) (solid blue) and Cross Calibrated Multi-Platform version 2 wind speed (CCMP2 WSP) (solid red) climatologies from the shaded 4° by 4° boxes. Shading, dotted lines, and solid black are as in Figure 6. SWARs include Western Australia (a) and (b), Central Western coast of South America near Chile (c) and (d), South-Western Coast of Africa near Namibia (e) and (f), and North-Western Arabian Sea (g) and (h). (Comparison plots showing equivalent quantities for WAVE-height, WATer depth and Current Hindcasting III (WW3) and IFREMER SWH and Climate Forecast System Reanalysis (CFSR) and CCMP2 WSP can be found in Figures S2b, S2d, S2f and S2g of the Supporting Information).
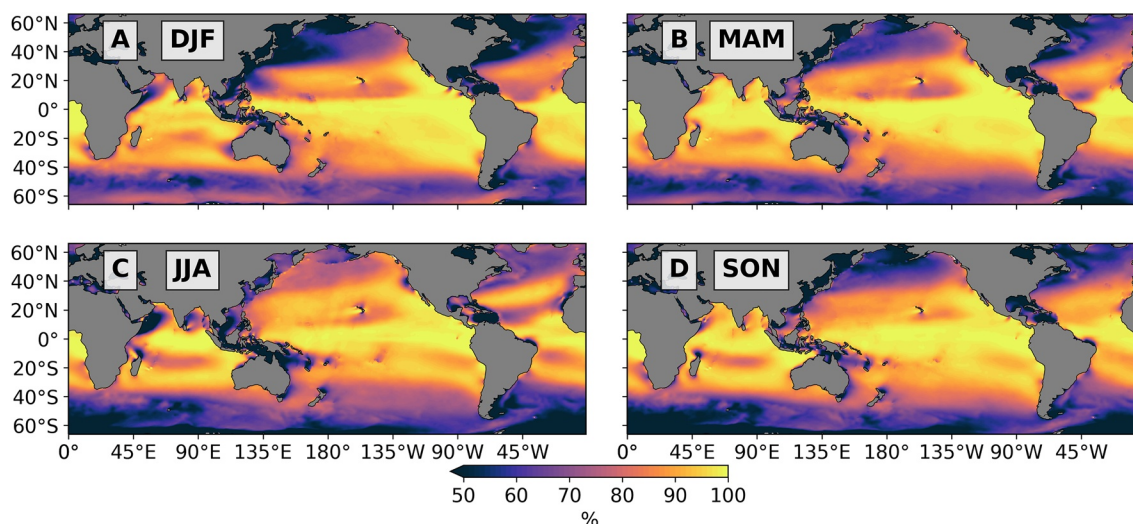
Figure 8. Seasonal progression of probability of swell using wave age criterion (Equation 3) and WW3 mean period $T_{m0,1}$ and WSP from January 1, 1993 to December 31, 2015 where (a) December-January-February (DJF), (b) March-April-May (MAM), (c) June-July-August (JJA), and (d) September-October-November (SON).

The seasonal progression of probability of swell (Figure 8) is consistent with the findings of Semedo et al. (2011). First we consider the expansion fan SWARs identified by Winant et al. (1988). In these regions, the wave field is dominated by wind-seas a higher percentage of time than it is in surrounding regions. Wind-seas occur most typically during the late spring and early summer months (Figures 8a and 8c). For the Northern Hemisphere, off the coasts of California and North Africa, the probability of swell drops to 70%–80% in spring and 50%–60% in summer. The Caribbean Sea has probabilities of swell below 50% through the entire year, with typical values ranging from 10%–40%, suggesting that the wave field consistently experiences stronger influence from local winds than most regions. In the Southern Hemisphere, the probability of swell in the SWARs of West Australia, Chile, and Namibia in the summer ranges from 70%–80%, which is not as low as in Northern Hemisphere SWARs. In the Arabian Sea, probability of swell drops to 40%–50% in the summer. These results are consistent with the hypothesis that the deviation from the basin-scale SWH annual cycle in SWARs results from locally forced wave contributions to SWH. The results also support the hypothesis that compared with the Northern Hemisphere SWARs, Southern Hemisphere SWARs are less likely to be dominated by locally forced waves because of their close proximity to persistent swell originating from the Southern Ocean.

One region of interest is the small coastal SWAR off the southern coast of Brazil near Rio de Janeiro (Figures 8a and 8d), where the probability of swell drops to 60%–70% during austral spring and summer. Although this SWAR was not identified by Winant et al. (1988), its low probability of swell during austral summer and its coastal location suggest that the region has characteristic traits of expansion fan wind regions and may in fact experience expansion fan winds despite being on a western boundary.

The second and third columns in Table 1 identify SWARs not identified as expansion fan regions by Winant et al. (1988) (see Figure 4). In these areas, the wave field is dominated by swell a high percentage of the time during the late spring, summer and early fall. The probability of swell is 95%–100% in these SWARs. This indicates that open-ocean and some coastal SWARs have regional wave and wind characteristics that are unfavorable for wind-seas.

4. Conclusion

In this paper, we have explored waves and winds separately, examining the seasonal cycle of WSP and SWH and closely examining regions where the seasonal cycles of winds and waves deviate from the seasonal cycle typically seen in the surrounding ocean basins. Atypical wave seasonal cycles are found within the equatorial region, where we see a sharp SWH phase transition, referred to as a swell phase discontinuity.

Atypical WSP seasonal cycles, out of phase with hemispheric-scale winds, are identified as SWARs and are located in eastern boundary current regions, monsoon regions, and regions significantly sheltered from remotely forced waves. In total, 3.39% of the world oceans from 66°S to 66°N latitude experience anomalous WSP seasonal variability.

The wave response to local winds is investigated to determine whether the characteristic features of the wind and wave fields observed off the California coast by Villas Bôas et al. (2017) are present in other SWARs. We find that most SWARs exhibit a 2–6 months phase difference between WSP and SWH annual cycles which is consistent with the California Coast SWAR. However, anomalous patterns of wind variability do not necessarily drive anomalous patterns of wave climatology as off the California Coast. Within potential expansion fan SWARs identified by Winant et al. (1988), SWH deviates from the SWH seasonal cycle in the Northern Hemisphere but shows a low-to-zero magnitude deviation in the Southern Hemisphere. Exceptions to these phasing patterns occur along the southern Mexican coast, in the South Caribbean, in monsoon regions, and on the Eastern Australian coast, where local winds dominate over hemispheric-scale seasonal wind patterns. In these regions, the wave climate is consistent with a response to local winds. While there are commonalities between SWARs, the fraction of wave variability attributed to local wind events varies depending on regional and wave field characteristics, suggesting that the statistics that define the coastal California SWAR are not universal, and each SWAR varies in slightly different ways depending on local conditions.

Probability of swell is used as a diagnostic to distinguish locally forced waves from remotely forced swell. Within SWARs associated with expansion fan winds, during spring and summer months, probability of swell is lower than in surrounding regions, implying wind-seas and SWH due to locally forced winds. This supports the hypothesis that the deviation from the SWH annual cycle results from waves that are forced by local wind events.

We have presented a method utilizing annual cycle phase to evaluate the relative importance of wind-sea and swell from mean behavior of the wave field without the need for directional wave spectra. Improved understanding of the SWH response to local wind events has the potential to lead to more accurate model representations of the wave climate in SWARs. In the future, global observations of directional wave spectra from remote sensing platforms such as the Chinese-French Oceanography Satellite CFOSAT and other proposed Doppler oceanography mission concepts have the potential to further our understanding of the effects of local winds on the wave climate: the addition of direction and frequency information would help to distinguish the roles of swell, wind-seas, and mixed seas in determining wave conditions under different wind regimes across the globe and to better quantify the contribution of local winds to regional wave climates.

Data Availability Statement

The data necessary to reproduce all results from this paper are publicly available through the University of California, San Diego library digital collections https://doi.org/10.6075/J06W9B6H. The source code used to produce the figures can be accessed on https://doi.org/10.5281/zenodo.4505581. Readers interested in accessing the raw data may visit http://www.remss.com/measurements/ccmp/ for the CCMP Version-2.0 vector wind analysis product, ftp://ftp.ifremer.fr/ifremer/cersat/products/swath/altimeters/waves for the satellite altimetry significant wave height product, and ftp://ftp.ifremer.fr/ifremer/ww3/HINDCAST for the WAVEWATCH 3 hindcast significant wave height, surface wind velocity, and peak wave frequency.

References

Alves, J. H. G., Banner, M. L., & Young, I. R. (2003). Revisiting the Pierson–Moskowitz asymptotic limits for fully developed wind waves. *Journal of Physical Oceanography*, *33*(7), 1301–1323. https://doi.org/10.1175/1520-0485(2003)033<1301:RTPALF>2.0.CO;2

Ardhuin, F. (2020). *Ocean waves in geosciences.* https://doi.org/10.13140/RG.2.2.16019.78888/5

Ardhuin, F., Stopa, J. E., Chapron, B., Collard, F., Jensen, R. E., Johannessen, J., et al. (2019). Observing sea states. *Frontiers in Marine Science*, *6*, 124. https://doi.org/10.3389/fmars.2019.00124

Atlas, R., Hoffman, R. N., Ardizzone, J., Leidner, S. M., Jusem, J. C., Smith, D. K., & Gombos, D. (2011). A cross-calibrated, multiplatform ocean surface wind velocity product for meteorological and oceanographic applications. *Bulletin of the American Meteorological Society*, *92*, 157–174. https://doi.org/10.1175/2010BAMS2946.1

Carter, D. J. T., Foale, S., & Webb, D. J. (1991). Variations in global wave climate throughout the year. *International Journal of Remote Sensing*, *12*(8), 1687–1697. https://doi.org/10.1080/01431169108955201

Cavaleri, L., Fox-Kemper, B., & Hemer, M. (2012). Wind waves in the coupled climate system. *Bulletin of the American Meteorological Society*, *93*(11), 1651–1661. https://doi.org/10.1175/BAMS-D-11-00170.1

Chen, G., Chapron, B., Ezraty, R., & Vandemark, D. (2002). A global view of swell and wind sea climate in the ocean by satellite altimeter and scatterometer. *Journal of Atmospheric and Oceanic Technology*, *19*(11), 1849–1859. https://doi.org/10.1175/1520-0426(2002)019<1849:AGVOSA>2.0.CO;2

Dodet, G., Piolle, J.-F., Quilfen, Y., Abdalla, S., Accensi, M., Ardhuin, F., et al. (2020). The sea state cci dataset v1: Towards a sea state climate data record based on satellite observations. *Earth System Science Data*, *12*(3), 1929–1951. https://doi.org/10.5194/essd-12-1929-2020

Donelan, M., Skafel, M., Graber, H., Liu, P., Schwab, D., & Venkatesh, S. (1992). On the growth rate of wind-generated waves. *Atmosphere-Ocean*, *30*(3), 457–478. https://doi.org/10.1080/07055900.1992.9649449

Draper, N. R., & Smith, H. (1998). *Applied regression analysis* (Vol. 326). John Wiley and Sons. https://doi.org/10.1002/9781118625590

Echevarria, E., Hemer, M., & Holbrook, N. (2019). Seasonal variability of the global spectral wind wave climate. *Journal of Geophysical Research: Oceans*, *124*(4), 2924–2939. https://doi.org/10.1029/2018JC014620

Edson, J., Crawford, T., Crescenti, J., Farrar, T., Frew, N., Gerbi, G., et al. (2007). The coupled boundary layers and air–sea transfer experiment in low winds. *Bulletin of the American Meteorological Society*, *88*(3), 341–356. https://doi.org/10.1175/BAMS-88-3-341

Gille, S. T. (2005). Statistical characterization of zonal and meridional ocean wind stress. *Journal of Atmospheric and Oceanic Technology*, *22*(9), 1353–1372. https://doi.org/10.1175/JTECH1789.1

Jiang, H., & Chen, G. (2013). A global view on the swell and wind sea climate by the Jason-1 mission: A revisit. *Journal of Atmospheric and Oceanic Technology*, *30*(8), 1833–1841. https://doi.org/10.1175/JTECH-D-12-00180.1

Munk, W. H. (1951). *Origin and generation of waves* (Tech. Rep.). Scripps Institution of Oceanography.

Press, W. H., Teukolsky, S. A., Flannery, B. P., & Vetterling, W. T. (1992). *Numerical recipes in fortran 77: Volume 1, volume 1 of fortran numerical recipes: The art of scientific computing*. Cambridge University press.

Queffeulou, P. (2004). Long–term validation of wave height measurements from altimeters. *Marine Geodesy*, *27*(3–4), 495–510. https://doi.org/10.1080/01490410490883478

Queffeulou, P., & Croizé-Fillon, D. (2017). *Global altimeter SWH data set* (Tech. Rep. Vol. 2). France: IFREMER.

Rascle, N., & Ardhuin, F. (2013). A global wave parameter database for geophysical applications. Part 2: Model validation with improved source term parameterization. *Ocean Modelling*, *70*, 174–188. https://doi.org/10.1016/j.ocemod.2012.12.001

Semedo, A. (2018). Seasonal variability of wind sea and swell waves climate along the canary current: The local wind effect. *Journal of Marine Science and Engineering*, *6*(1), 28. https://doi.org/10.3390/jmse6010028

Semedo, A., Sušelj, K., Rutgersson, A., & Sterl, A. (2011). A global view on the wind sea and swell climate and variability from ERA-40. *Journal of Climate*, *24*(5), 1461–1479. https://doi.org/10.1175/2010JCLI3718.1

Snodgrass, F. E., Hasselmann, K. F., Miller, G. R., Munk, W. H., & Powers, W. H. (1966). Propagation of ocean swell across the Pacific. *Philosophical Transactions of the Royal Society of London - Series A: Mathematical and Physical Sciences*, *259*(1103), 431–497. https://doi.org/10.1098/rsta.1966.0022

Stopa, J. E. (2019). Seasonality of wind speeds and wave heights from 30 years of satellite altimetry. *Advances in Space Research*, *68*(2), 787–801. https://doi.org/10.1016/j.asr.2019.09.057

Stopa, J. E., Ardhuin, F., & Girard-Ardhuin, F. (2016). Wave climate in the Arctic 1992–2014: Seasonality and trends. *The Cryosphere*, *10*, 1605–1629. https://doi.org/10.5194/tc-10-1605-2016

Stopa, J. E., & Cheung, K. F. (2014). Periodicity and patterns of ocean wind and wave climate. *Journal of Geophysical Research: Oceans*, *119*(8), 5563–5584. https://doi.org/10.1002/2013JC009729

Sullivan, P. P., McWilliams, J. C., & Melville, W. K. (2004). The oceanic boundary layer driven by wave breaking with stochastic variability. Part 1. Direct numerical simulations. *Journal of Fluid Mechanics*, *507*, 143–174. https://doi.org/10.1017/S0022112004008882

Sverdrup, H. U., & Munk, W. H. (1947). *Wind, sea and swell: Theory of relations for forecasting* (No. 303). Hydrographic Office. https://doi.org/10.5962/bhl.title.38751

Villas Bôas, A. B., Ardhuin, F., Ayet, A., Bourassa, M. A., Brandt, P., Chapron, B., et al. (2019). Integrated observations of global surface winds, currents, and waves: Requirements and challenges for the next decade. *Frontiers in Marine Science*, *6*. https://doi.org/10.3389/fmars.2019.00425

Villas Bôas, A. B., Gille, S. T., Mazloff, M. R., & Cornuelle, B. D. (2017). Characterization of the deep water surface wave variability in the California Current region. *Journal of Geophysical Research: Oceans*, *122*(11), 8753–8769. https://doi.org/10.1002/2017JC013280

Winant, C. D., Dorman, C. E., Friehe, C. A., & Beardsley, R. C. (1988). The marine layer off northern California: An example of supercritical channel flow. *Journal of the Atmospheric Sciences*, *45*(23), 3588–3605. https://doi.org/10.1175/1520-0469(1988)045<3588:TMLONC>2.0.CO;2

Young, I. R. (1999). Seasonal variability of the global ocean wind and wave climate. *International Journal of Climatology: A Journal of the Royal Meteorological Society*, *19*(9), 931–950. https://doi.org/10.1002/(SICI)1097-0088(199907)19:9<931::AID-JOC412>3.0.CO;2-O

Young, I. R., Fontaine, E., Liu, Q., & Babanin, A. V. (2020). The wave climate of the Southern Ocean. *Journal of Physical Oceanography*, *50*(5), 1417–1433. https://doi.org/10.1175/JPO-D-20-0031.1

Young, I. R., Zieger, S., & Babanin, A. V. (2011). Global trends in wind speed and wave height. *Science*, *332*(6028), 451–455. https://doi.org/10.1126/science.1197219

Zheng, K., Sun, J., Guan, C., & Shao, W. (2016). Analysis of the global swell and wind sea energy distribution using Wave watch III. *Advances in Meteorology*, *2016*, 1–9. https://doi.org/10.1155/2016/8419580